Catalysis Science & Technology

Accepted Manuscript

ROYAL SOCIETY OF CHEMISTRY

www.rsc.org/catalysis

Journal Name

RSCPublishing

ARTICLE

PdFe nanoparticle as a selective catalyst for C-C cleavage in hydrogenolysis of vicinal diol units in biomass derived chemicals

Cite this: DOI: 10.1039/xoxxoooooox

Received ooth January 2012,
Accepted ooth January 2012

DOI: 10.1039/xoxxoooooox

www.rsc.org/

Fenglin Liao [a], Tsz Woon Benedict Lo [a], Douglas Sexton [a], Jin Qu [a], Cheng-tar Wu [a] and Shik Chi Edman Tsang [a] *

A series of supported PdFe bimetallic nanoparticles with variable composition are synthesized successfully through careful reduction of PdO/FeO_x complex with tunable support structure, which are demonstrated to achieve ultra-selective C-C bond cleavage over C-O bond of vicinal diol units in the hydrogenolysis of biomass derived molecules: a progressive increase in Fe(0) content of the bimetallic nanoparticles suggested by EXAFS analysis and DFT calculations is shown to give more enhanced selectivity of C-C cleavage until reaching 95%.

1 Introduction:

Currently, the energy and chemical provisions heavily rely on non-renewable fossil fuels which are neither secured, nor sustainable sources.[1,2] With ever increasing energy demand but continuously lowering of natural reserves, these non-renewable routes are unlikely to last for a long time. [3,4,5,6] Renewable resources, including hydro power, wind, solar and biomass, are therefore becoming increasingly important for sustainable development.[1] Due to the large contribution to the global primary energy (up to 40% in some countries), biomass is recently advocated as one of the main alternatives in the United National Conference on Environment and Development. [7] However, the direct use of biomass is limited and thus, catalytic conversion of biomass molecules to value-added chemicals is required. For example, the conversion of biomass molecules to small alcohol molecules (methanol, ethanol, etc.) in hydrogen is desirable as these volatile high energy density liquids can be widely used for both energy consumption (as transportation fuels) and chemical synthesis. [5] Methanol can be produced from biomass industrially by a two-step process; the first step is the gasification of biomass to "synthesis gas" containing CO and H_2, which is then converted into methanol. [8] However, this process requires a temperature at or above 850 °C to break down the biomass molecules to synthesis gas, followed by its reformation to methanol at 200-250 °C. Therefore, this is a highly energy inefficient process. Meanwhile, the production of ethanol from sugarcane and corn by the biological fermentation method is known for several thousands of years, but this process is not only food dependent, but is also very slow. [9-11] As a result, a new and direct transformation of biomass and derived chemicals (cellulose, sugar, glycerol, etc.) into valuable small alcohol molecules over inorganic based catalyst would be commercially attractive. [12-16] Most biomass molecules exist in the form of $-(CHOH)_n-$ chain. Thus, from the viewpoint of molecular structure, the breakdown of these biomass molecules to small alcohol molecules must be achieved through the hydrogenolytic cleavage of C-C bond in –(CHOHCHOH)- with the vicinal diol units. However, much current research has been focused on hydrogenolytic C-O cleavage for the production of liquid alkanes as fuels despite the rapid C-C cleavage accompanying the C-O cleavage always leads to the formation of undesirable light alkanes. [17,18] Thus, there is only limited literature exploring the production of small alcohol molecules directly from biomass, which involves the selective C-C cleavage of vicinal diol units. The development of this catalysis reaction is very challenging since any low selectivity for C-C over C-O cleavage of the catalytic process does not only cause light alkanes formation, but also gives a wide products distribution that causes separation problem [19,20] (note their similar homolytic cleavage energies; ΔH_{C-C} 348 kJ/mol and ΔH_{C-O} 360 kJ/mol). Thus, in order to produce small alcohol molecules efficiently from biomass substrates, a new catalyst with a high selectivity for C-C over C-O cleavage is needed.

Pd/FeOx catalyst containing small supported PdFe nanoparticles of low Fe content upon in-situ reduction was reported previously by our group to be highly active in breaking down ethylene glycol molecule, the simplest biomass related molecule with basic –CHOH-CHOH- unit in hydrogen, without the production of methane. [19] The liquid products were mainly composed of a mixture of methanol (the product of C-C cleavage) and ethanol (the product of C-O cleavage) with combined selectivity of above 75% but no specific C-C cleavage over C-O cleavage was obtained. When it was tested for the hydrogenolysis of glycerol, a range of products, including ethylene glycol, 1,2-propandiol, 1-propanol, methanol, ethanol with comparable concentrations, was also obtained. [20]

Here, we report that by blending a variable concentration of Zn(II) into Pd/FeO_x during the synthesis (precipitation followed by controlled reduction, see the experimental section), a series of extremely small supported PdFe bimetallic nanoparticles of similar size but with controllable Fe content can be prepared. It is found that the progressive increase in Fe content of PdFe dependent on Zn(II) incorporation will lead to higher catalytic C-C cleavage over C-O cleavage in hydrogenolysis of ethylene glycol. The high specificity for hydrogenolytic C-C bond fission of this new catalyst is also demonstrated for other 1,2-diols and glycerol molecule.

2 Experiment:

2.1 Catalyst preparation:

The PdFe bimetallic clusters were produced through the reduction of PdO/Fe_2O_3. Zn(II) was added to facilitate the reduction of Fe ions to Fe(0) from the support, which dictated the ratio of Pd:Fe in the bimetallic clusters. First, solutions of $Zn(NO_3)_2.6H_2O$ (50 mL) and $Fe(NO_3)_3$ (200 mL) in various concentrations were prepared. Next, 10 mL Na_2CO_3 solution (1 M) was slowly added into the 50 mL $Zn(NO_3)_2$ solution to generate a white suspension of $Zn(OH)_x$, the obtained mixture was then added drop-wise into the 200 mL $Fe(NO_3)_3$ solution to form a reddish gel-like solution. The pH of the final gel was adjusted to 4 by adding 1 M Na_2CO_3 solution. Then, the reddish gel was added slowly into a solution of 200 mL $Pd(NO_3)_2$ (0.05 wt% Pd), and the pH of this mixture was adjusted to 9 by further adding 1 M Na_2CO_3 solution. The final mixture was stirred overnight and the solid product was harvested by centrifugation. The solid was rinsed with copious amount of water in order to remove any residual sodium ion before it was dried in oven at 80 °C. Before pre-reduction, the samples were calcined at 300 °C for 2 h to generate PdO/Fe_2O_3 complex. Then, they were placed in a 3 necked flask to be reduced at 250 °C with a H_2 flow of 30 ml/min for 1 h.

2.2 Catalyst characterization:

Inductive coupled plasma – atomic emission spectrometry (ICP-AES) was performed on an IRIS Intrepid II XSP spectrometer. X-ray diffraction (XRD) data was collected using a Philips PW1729 diffractometer, operating in Bragg-Brentano focusing geometry and using Cu Kα radiation (λ = 1.5418 Å) from a generator operating at 40 kV and 30 mA. Diffusion reflectance spectroscopy (DRS) was employed to determine the band structure of the catalyst and the data was collected on a Perkinelmer Lambda 750S Uv/vis spectrometer. Photoluminescence (PL) spectra were recorded by HORIBA JOBINYVON iHR320 with a Kimmon He-Cd laser; the excitation wavelength was set at 380 nm. X-ray photoelectron spectroscopy (XPS) was performed on Kratos Ltd XSAM800 and the whole procedure including the loading of the reduced samples are protected in N_2 without exposure to air. Transmission electron microscopy (TEM) images were obtained using a JEOL 2021F microscope operating at 200 kV equipped with a post-column Gatan imaging filter (GIF-Tridium). The samples were prepared by placing a drop of nanoparticle-ethanol suspension onto a carbon-coated copper grid, then allowing the solvent to evaporate.

Temperature programmed reduction (TPR) was used to investigate the reduction behaviour of the catalysts. The data was collected on a Thermo-Quest TPRO 110 instrument. Inside the TPR quartz tube, 0.01 g of the calcined catalyst sample (at 300 °C) was sandwiched between two layers of quartz wool with a thermocouple placed in contact with the top layer quartz wool. The TPR tube was then inserted into the instrument for a pre-treatment (helium running through the TPR tube at 10 mL/min at a temperature ramp of 10 °C/min from 40 °C up to 150 °C, then held for 5 minutes before cooling). The helium pre-treatment cleaned the catalyst surface by removing the absorbed ambient gas molecules. After the pre-treatment, a reduction treatment (5% H_2 in argon flowing through the TPR tube at 20 mL/min at a temperature ramp of 10 °C/min from 40 °C up to 800 °C) was carried out in order to observe the reduction process of the catalysts.

Extended X-ray absorption fine structure (EXAFS) measurements at the Pd K-edge (24530 eV) were performed on beamline B18 at Diamond Light Source (Diamond, UK) to obtain information about the local structure of Pd (nearest-neighbour inter-atomic distances and coordination number). The Diamond installation comprises a 3 GeV electron storage ring with typical current of 200 mA. Beamline B18 is a bending magnet which has been designed to deliver monochromatic X-rays in the energy range of 2 to 35 keV. A Si (311) double crystal monochromator was used for energy selection with a resolution of 1 eV. X-ray absorption spectroscopy data were collected at ambient temperature in transmission mode using optimized ionization chambers as the detectors. The EXAFS data analysis was performed using IFEFFIT 1 with Horae packages 2 (Athena and Artemis). All spectra were calibrated with the Pd foil reference to avoid small energy shifts of the nanocatalyst. The amplitude parameter was obtained from EXAFS data analysis of Pd foil with a known coordination number equals to 12, which was used as a fixed input parameter in all fits to allow coordination number (CN) refinement. In the fitting process of experimental data, we have only performed the first shell data analysis under the assumption of a single scattering. The curve-fitting analysis was done in k^3 space with a range of 2-12. The errors in analysis were estimated by R-factors.

2.3 Modelling computation:

Modelling computation was employed to appreciate the electronic properties of PdFe bimetallic particles. All calculations were performed in the framework of DFT by using the Vienna ab initio simulation package (VASP 4.6) [21-23]. The projector-augmented wave (PAW) potentials [24,25] were used for the core electron interaction. The Perdew–Burke–Ernzerhof (PBE) [26,27] based on the generalized gradient approximation(GGA) was employed to evaluate the non-local exchange-correlation energy. A plane wave basis set with a cutoff energy of 350 eV was used. For structure optimization, the ionic positions were allowed to relax until the forces became less than 0.05 eV/Å. Spin polarization was included for all the calculations. The most abundant close-packed Pd(111) surface was modelled by a periodic slab model with four layers of metals. A 4×4 surface unit cell (11.171 × 11.171 $Å^2$) and a 3×3×1 k-point grid determined by the Monkhorst-Pack method were utilized in this study. The bottom layer was fixed during all geometry optimizations. A vacuum layer of 15 Å along the z direction perpendicular to the surface (the x and y directions parallel to the surface) was employed to prevent spurious interactions between the repeated slabs. Some Fe impurities were induced to substitute for surface Pd atoms to study the modification effects on Pd(111). The non-segregated surface alloy model[28] was used here as showed in Scheme 1.

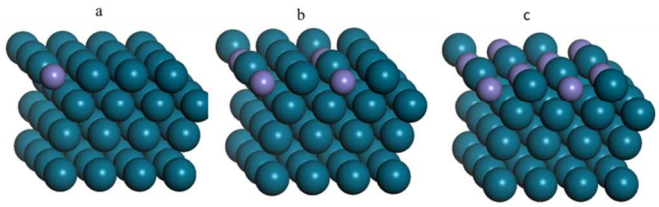

Scheme 1. Surface alloy models: a) $Pd_{15}Fe$; b) Pd_3Fe; c) PdFe. Blue balls represent Pd atoms, while purple balls, Fe atoms

2.4 Catalysis tests:

The hydrogenolysis reactions were carried out in liquid phase using a 160 mL autoclave. In a typical experiment, 30 mL of substrate solution and 0.5 g freshly reduced catalyst were loaded into the reactor inside a glove box. The reactor was flushed with pure (99.9%) hydrogen gas to remove any trace

amount of air. The autoclave was pressurized to 50 bar with hydrogen gas at room temperature, after which it was heated up to 250 °C to allow the reaction to proceed with constant stirring. The conversion, product selectivity and the value of "Selective C-C cleavage: Selective C-O cleavage" are calculated as following:

$$\text{Conversion} = \frac{\text{moles of glycerol in reactants} - \text{moles of glycerol in the mixture after reaction}}{\text{moles of glycerol in reactants}}$$

$$\text{Selectivity} = \frac{\text{moles of specific product} * \text{its mole carbon number}}{\sum \text{moles of each product} * \text{its mole carbon number}}$$

$$\frac{\text{selective C} - \text{C cleavage}}{\text{selective C} - \text{O cleavage}} = \frac{\text{moles of glycerol needed to produce the selective C} - \text{C cleavage product}}{\text{moles of glycerol needed to produce the selective C} - \text{O cleavage product}}$$

3 Results and discussion:

3.1 Characterization of the catalysts:

Zn(II) was added to modify the structure of the primary PdO/Fe_2O_3 complex and the Zn concentration was determined by ICP-AES as shown in Table 1.

Table 1. The compositions of a series zinc modified PdO/Fe_2O_3 before the pre-reduction (the loading of Pd is around 5 wt%).

Sample	Mass of added $Zn(NO_3)_2.6H_2O$ (g)	Mass of added $Fe(NO_3)_3.9H_2O$ (g)	Weight % of Zn
1	0.00	10.41	0.00
2	1.18	7.90	11.8
3	1.48	7.50	13.5
4	2.29	6.40	20.8

Temperature programmed reduction (TPR) was used to investigate the detailed reduction behaviour of the zinc blended samples; the curves are shown in Fig. 1a. The two characteristic TPR peaks are assigned to the reduction of iron oxide which are taken place in two steps: $Fe_2O_3 \rightarrow Fe_3O_4$ and $Fe_3O_4 \rightarrow Fe(0)$; the reduction of PdO to Pd is known to readily take place at sub-ambient temperature. The second step is clearly taken place above 300 °C[19] corresponding to the second peak in TPR curves, while the first peak is related to the transformation of Fe_2O_3 to Fe_3O_4. For sample 1, the calculated value of H_2 consumption for the first peak around 100 °C (2.4 mmol/g) is slightly higher than the theoretical value for the transformation of all the Fe_2O_3 to Fe_3O_4 (2.1 mmol/g), which means the support can be reduced to Fe_3O_4 completely in the pre-reduction at 250 °C. This deduction is confirmed by the result of X-ray diffraction (XRD) (Fig. 1b); all the diffraction peaks in the pattern of reduced sample 1 can be indexed to Fe_3O_4 [29, 30]. However, as shown in Fig. 1a, with the addition of Zn(II), the H_2 consumptions of all the samples under 250 °C increase dramatically. The values become much higher than the theoretical value for $Fe_2O_3 \rightarrow Fe_3O_4$, which suggests that some surface Fe_3O_4 in contact with Pd(0) should have been further converted to Fe(0) in the first step. The H_2 consumption reaches maximum at sample 3 (13.5 wt% Zn) which alludes to the highest concentration of Fe(0) in this reduced catalyst. The amount of Fe(0) is calculated according to reaction stoichiometry and the result is shown in Table 2. Zn(II) will not be reduced in the presence of Fe(II) due to the much more negative reduction potential of Zn(II) to Zn(0) than that of Fe(II) to Fe(0) (E^0[Zn(II)/Zn(0)] = -0.76 eV, E^0[Fe(II)/Fe(0)] = -0.44 eV). Thus, with increasing concentration of Zn(II), the diffraction peaks for ZnO (31.8°, 34.4°) become more significant as shown in Fig. 1b.

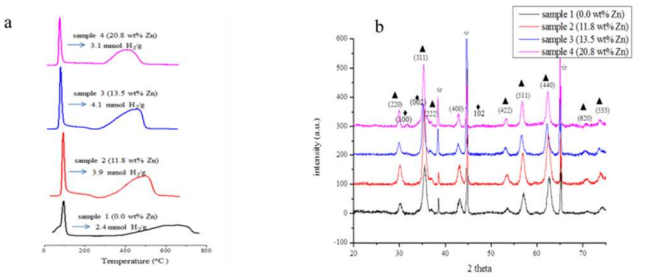

Fig. 1. a) TPR of a series of zinc modified PdO/Fe_2O_3 samples and hydrogen consumptions (calculated by the integrated areas of first peaks); b) XRD diffractograms of the samples after pre-reduction (▲ Fe_3O_4, ♦ZnO, ☆Al sample holder).

Table 2. The calculated amount of produced Fe(0) from TPR for the zinc modified PdO/Fe_2O_3 samples.

Sample	1 (Zn 0.0wt%)	2 (Zn 11.8wt%)	3 (Zn 13.5wt%)	4 (Zn 20.8wt%)
Produced Fe (mmol/g)	0.23	1.67	1.97	1.39

The X-ray photoelectron spectroscopy (XPS) curves of Fe 2p for a series of reduced sample are shown in Fig. 2. The binding energies of Fe $2p_{3/2}$ clearly show a decrease trend, with sample 1 > sample 4 > sample 2 > sample 3. It is noted that the literature values for Fe(0) $2p_{3/2}$ and Fe_3O_4 $2p_{3/2}$ are 707.7 eV and 710.2 eV, respectively [31, 32]. Therefore, the binding energy is found to decrease with the increasing concentration of Fe(0). For sample 1 (without the addition of zinc), the binding energy of Fe $2p_{3/2}$ is 710.0 eV, which agrees with the literature value of Fe_3O_4. The much lower values of binding energies in samples 2 (11.8 wt% Zn) and 3 (13.5 wt% Zn) indicate that the concentrations of Fe(0) are higher; this suggests that there is indeed a further reduction of Fe_3O_4 to Fe(0) which is consistent with the results of TPR. The strong peak at 707.8 eV in the fitting XPS curve for sample 3 (13.5 wt% Zn) indicates that the concentration of Fe(0) in this sample is significantly high.

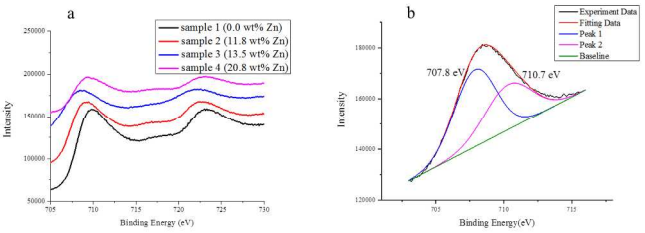

Fig. 2. a) XPS curves of Fe 2p of the reduced samples 1-4; b) XPS curve fitting of Fe 2p for sample 3 (13.5 wt% Zn).

The combined results of TPR, XRD and XPS confirm that the formation of Pd atoms upon hydrogen reduction can selectively assist further reduction of Fe ions (in the support) to metallic Fe(0) with the assistance of blended Zn(II) at around 100 °C. A series of the characterization techniques were employed to investigate how the addition of zinc influences the reduction behaviour of the Fe_2O_3 support. The XRD diffractograms of samples 1-4 before reduction with variable zinc concentration are displayed in Fig. 3a. The diffractograms suggest that all the samples can be indexed and identified to the spinel structure (space group: Fd-3m). It is well known that γ-Fe_2O_3 has a typical spinel structure in which O^{2-} are cubic closed packed while the Fe(III) occupy 1/8 tetrahedral sites and 1/2 octahedral sites. [33] When Zn(II) is blended to the system,

some Fe(III) at the tetrahedral sites will be replaced, while the spinel structure is maintained. From empirical calculation, when all the Fe(III) at the tetrahedral sites are substituted by Zn(II), a stable $ZnFe_2O_4$ phase can be formed, at which the concentration of zinc is 21.2 wt%. Beyond this value, the ZnO phase will be formed. The concentrations of zinc determined by ICP-AES in the samples are below this value, thus there is no diffraction peak of ZnO observed and the samples should compose of a mixture of $ZnFe_2O_4$ and γ-Fe_2O_3 with the same lattice structure. The calculated ratio of $ZnFe_2O_4$: Fe_2O_3 from the results of ICP-AES are displayed in Table 3.

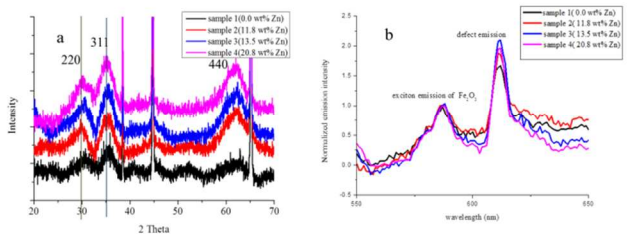

Fig. 3. a) XRD diffractograms; b) Normalized PL spectra of a series of Zn(II) blended samples before pre-reduction.

Table 3. The calculated mole ratio of $ZnFe_2O_4$: Fe_2O_3 for the series of zinc modified samples from ICP-AES.

Sample	1 (0.0 wt% Zn)	2 (11.8 wt% Zn)	3 (13.5 wt% Zn)	4 (20.8 wt% Zn)
$ZnFe_2O_4$: Fe_2O_3	0	0.6	1.0	8.6

Static photoluminescence (PL) spectroscopy was employed to observe the surface state of the catalysts. As shown in Fig. 3b, two emission peaks locating at 570 nm and 630 nm are observed in all the spectra. The former one is due to the characteristic excitons recombination of γ-Fe_2O_3, while the other one with longer wavelength should be assigned to the emission associated with surface defects of the material [34]. It is noted that the intensity of the second peak increases with the addition of zinc and reaches maximum at sample 3 (13.5 wt% Zn), which suggests that it has the greatest amount of defective states on the surface. When a small amount of zinc compound is introduced into the system, the adjacent iron oxide area is transformed into the $ZnFe_2O_4$ spinel phase in the calcination process through the diffusion of ions. Meanwhile, the iron oxide area that is far away from the zinc rich area maintains at its original state. Thus, in the calcined product, the distribution of Fe among the lattice becomes uneven due to the co-existence of adjacent $ZnFe_2O_4$ and Fe_2O_3. Consequently, the lattice strain and the number of defects increase at the interface, as supported by the fact that a greater emission at longer wavelength was observed. The strongest emission peak at 630nm is then observed at sample 3 (13.5 wt% Zn) due to the 1:1 ratio of $ZnFe_2O_4$:Fe_2O_3, at which the amount of interfaces between the two phases is maximized. With continuous addition of zinc oxide seeds, more and more Fe(III) at tetrahedral site are replaced by Zn(II) until the whole structure is transformed into $ZnFe_2O_4$. Ultimately, the concentration of surface defect decreases gradually.

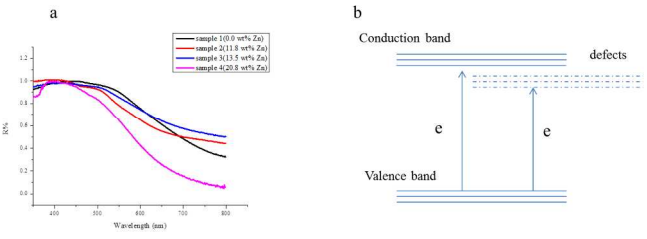

Fig. 4. a) Normalized DRS curves for a series of zinc modified PdO/Fe_2O_3 catalysts; b) The band structure of semi-conductor with defective surface.

Table 4. The band gap values of the supports for a series of zinc modified PdO/Fe_2O_3 catalysts.

Sample	1 (0.0 wt% Zn)	2 (11.8 wt% Zn)	3 (13.5 wt% Zn)	4 (20.8 wt% Zn)
Band gap (eV)	1.80	1.77	1.69	1.97

Fig. 4a displays the diffusion reflectance spectroscopy (DRS) curves for all the samples. After normalizing the data, it is noted that sample 3 shows the strongest absorption in the visible-infrared region indicating that it has the narrowest band gap. The value of band gap can be determined by Tauc equation and the results are shown in Table 4. The smallest value of sample 3 can be explained by its most defective surface; the defects provide some trap sites for the excited electrons which are located under the position of conduction band as shown in Fig. 4b, and a narrower band gap is observed. The trap of excited electrons by the surface defects facilitates the elimination of the holes as [O] of lower charge than formal -2 charge by H_2, which then promotes the reduction of iron ions into Fe(0) by the excited electrons. With the combined results of XRD, PL and DRS for the samples before reduction, it is concluded that the introduction of appropriate amount of zinc ions into the lattice of Fe_2O_3 renders the semiconductive structure to be more defective, and therefore, the Fe(III) will become more prone to be reduced to Fe(0).

Given the fact Pd is active site facilitating the catalytic reduction of Fe iron to Fe(0), supported PdFe bimetallic nanoparticles are expected to be formed at the interface through the interaction of Pd and Fe atoms. The extended X-ray absorption fine structure (EXAFS) results of the samples at Pd K edge are shown in Fig. 5 and Table 5. The total coordination number (CN) (5.3-6.5) of Pd in these samples suggests that the metallic Pd containing phase produced by this method is extremely small in size. We have estimated the average size of the Pd nanoparticles to be 1.0-1.5 nm from the analysis of the total CN derived by EXAFS data within acceptable R (fitting factor) and Debye-Waller factors, based on the calibration model of a recent EXAFS study alongside with other multiple techniques, including gas adsorption, TEM and XRD [35, 36]. (Noted that our commercial Pd/C with 2 nm Pd particles give a CN of ca. 8.0 at Pd–Pd distance of 2.73 Å from the first shell analysis, which is fitted well in the reported calibration curve.) Another striking feature that we noted in EXAFS is the direct observation of a shorter scattering path at 2.58 Å comparing with the typical Pd–Pd distance at 2.70 Å [37] after reduction (kept in inert atmosphere). The distance of 2.58 Å represents the first shell neighbour Fe atoms around each Pd absorbing atom (number of neighbour Fe ranges from 0.7 to 2.4). The shorter distance of Pd-Fe is arisen due to the smaller size of Fe than that of Pd. It is very interesting to find that the numbers of neighbour Fe (NFe) around Pd absorbing atom are controllable dependent on the concentration of Zn(II) added to the precursors, which is indicative of the tailoring ability on the composition of the bimetallic particles (samples 1 to 4). Sample 3 (13.5 wt% Zn) gives the highest number of first shell neighbour Fe

to Pd followed by sample 2 > sample 4 > sample 1 reflecting the variable composition of PdFe nanoparticles, which is consistent with the results of TPR and XPS.

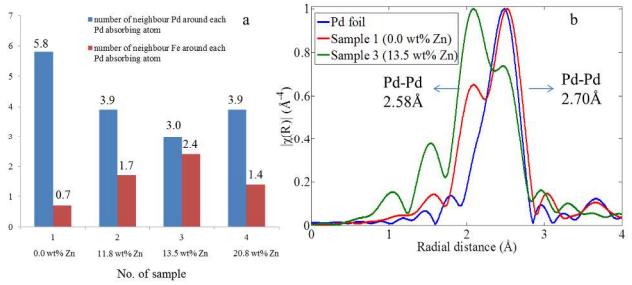

Fig. 5. a) Number of neighbour Pd (NPd) and Fe atoms (NFe) around each Pd absorbing atom derived from EXAFS fittings; b) the Fourier transform of the EXAFS curves (typical EXAFS curves against radial distance) for sample 1 (0.0 wt% Zn) and sample 3 (13.5 wt% Zn) with a reference of Pd foil (note: the labelled concentration of Zn indicates the content of Zn in the catalyst before pre-reduction).

Table 5. Average coordination environment of a Pd absorbing atom from the EXAFS results for the reduced zinc modified Pd/Fe_2O_3 samples.

Sample	Total CN	Enot (eV)	Pd-Pd distance (Å)	D-W factor ($Å^2$)	Pd-Fe distance (Å)	D-W factor ($Å^2$)	R
1	6.5(3)	2.0	2.70(2)	0.009(1)	2.60(1)	0.006(1)	0.5%
2	5.8(6)	1.0	2.71(1)	0.011(1)	2.56(1)	0.006(1)	0.9%
3	5.4(6)	-2.0	2.69(1).	0.009(1)	2.58(1)	0.013(1)	2.5%
4	5.3(4)	1.1	2.71(1)	0.014(1)	2.56(1)	0.004(1)	0.9%

("CN" is coordination number; "Enot" is the energy difference between the experimental absorption energy and the calculated value in curve fitting; "D-W" is Debye Waller; "R" factor is the indication of the quality of curve fitting)

Transmission electron microscopy (TEM) was conducted to visualize the Pd containing metal particles. From Fig. 6, the images show that the structure and the shape of the particles are irregular in the samples 1 and 3 with no significant difference in the morphology. From the high resolution images, clear lattice fringe separations of 0.23 nm of metal particles were found in both of the two samples which can be assigned to the (111) plane of Pd or PdFe particles. From the particle size distribution diagram, the average size of metal particles is around 1-3 nm (with mean size of 1.5 nm), which is almost the same for the two samples and also consistent with the estimations from the EXAFS data. Thus the addition of Zn(II) only influences the composition of the supported PdFe nanoparticles, but keeps the particle size unchanged.

It is thought that the electronic properties of Pd may be modified by the Fe atoms in proximity with the formation of PdFe bimetallic nanoparticles. Thus, Pd 3d XPS characterization was closely examined for the H_2 reduced samples with reference to adventurous carbon (284.4 eV; no exposure to air), which are displayed in Fig. 7a. It is observed that the Pd $3d_{5/2}$ binding energy values of samples 2 and 3 which have higher content of Fe(0) (as shown in Fig. 5a) are significantly lower than that of sample 4, followed by sample 1. Owing to the lower electronegativity, Fe is more prone to lose its electrons to Pd (1.8 and 2.2 for Fe and Pd atom, respectively). Thus, when Pd is placed in a close proximity to Fe atoms in the

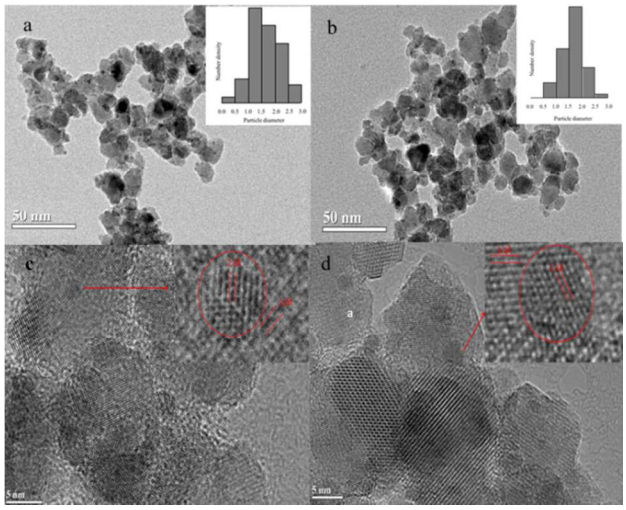

Fig. 6. (a, b) TEM and (c,d) HRTEM images for reduced sample 1 (0.0 wt% Zn) (a,c) and sample 3 (13.5 wt% Zn) (b,d) (the labeled distance of 3.0 Å corresponds to inter-planar distance of the (112) plane of Fe_3O_4 [38]).

bimetallic structure, a downshift in the binding energy of Pd at increasing concentration of Fe(0) is clearly observed. The influence of Fe atom on the electronic properties of Pd particles is also appreciated by the density functional theory (DFT) calculations based on a 4x4x4 atomistic model with Fe substitution on the top layer (see scheme 1). The relative position of surface d-band fillings and d-band centers for Pd, $Pd_{15}Fe$, Pd_3Fe and PdFe (all with face center cubic (fcc) structure) with a fixed lattice parameter are compared and displayed in Fig. 7b and the corresponding diagrams of surface density of states are shown in Fig. 8. It is revealed that the d-band filling decreases at higher degree of Fe substitution. This is consistent with the prediction from the d-band center theory that the center gravity of d-band filling will shift to lower value for the 'hybrid' (HOMO) d-band of PdFe, owning to the mixing of Fe 3d with Pd 4d (Pd ($4d^{10}5s^2$) has lower d-electron number than Fe ($3d^64s^2$)). [39] It is also noted that the d-band center position shifts downward at high content of Fe despite the higher energy level of Fe 3d comparing to that of Pd 4d. This is attributed to the dominant effect of decreasing d-band filling over theoretical upshift in d-band center. (Note that the d-band center position rises slightly at a very low Fe content, which is initially dominated by the effect of hybridization with the higher energy orbital of Fe 3d than that of Pd 4d)

3.2 Catalytic results of the PdFe samples in the hydrogenolysis of a series of diols and glycerol

The supported PdFe nanoparticles were tested for the hydrogenolysis of ethylene glycol (EG) and the results are displayed in Table 6 and Fig. 9. The main products included methanol, ethanol and CO2 as similar to our previous results obtained over Pd/FeOx catalyst tested at milder conditions (lower pressure and temperature). [19] Although the CO2 selectivity at present is higher than the previous data (hence lower alcohols selectivity), higher degree of C-C and C-O cleavages can be obtained at shorter experimental time for a clearer comparative purpose. From the molecular configuration, methanol is the product of hydrogenolytic C-C cleavage of ethylene glycol and ethanol is the product of C-O cleavage, while CO_2 is formed by steam reformation of surface carbonaceous species.[40] Thus, the selectivities of methanol and ethanol reflect the catalytic ability of the PdFe bimetallic nanoparticles in selectively breaking C-C and C-

O bond of the vicinal diol, respectively. It is noted that methanol selectivity increases with the number of neighbour Fe around Pd absorbing atom in PdFe bimetallic nanoparticles at the expense of ethanol selectivity (Fig. 9a), which suggests the specificity for cleavage of C-C bond over C-O bond progressively increases. The value of "Selective C-C cleavage: Selective C-O cleavage" for the catalysts can be calculated from the mole ratio of methanol to ethanol in the

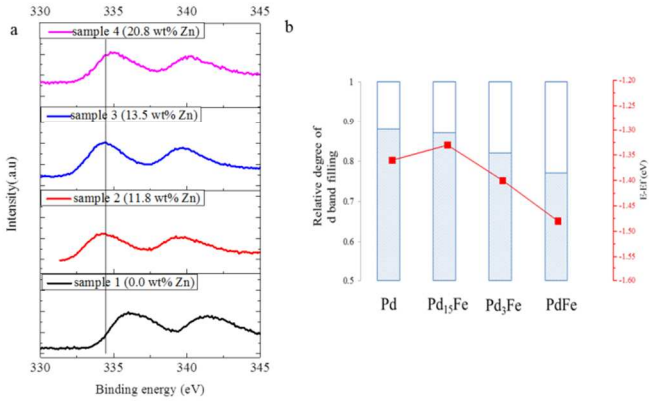

Fig. 7. a) XPS of Pd 3d of the reduced Pd samples, b) Calculated d-band filling (blue bar) and d-band center position (red dot) for the surface of pure Pd, $Pd_{15}Fe$, Pd_3Fe and PdFe.

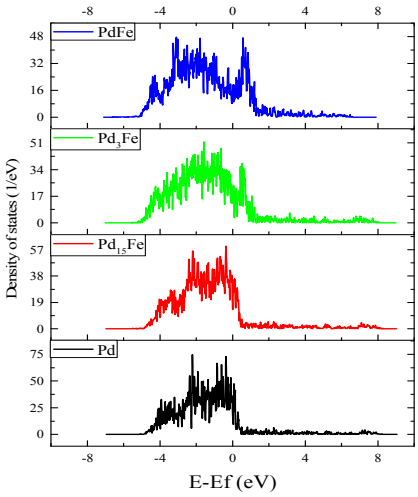

Fig. 8. Calculated surface density of states (SDOS) diagrams of Pd, $Pd_{15}Fe$, Pd_3Fe, PdFe.

liquid products. As shown in Fig. 9b, the value increases basically linearly with the concentration of Fe(0) in PdFe until levelling at 16.4 in the sample 3 (13.5 wt% Zn) with the highest Fe(0) content; this means that the selectivity of C-C cleavage in the reaction reaches 95% (16.4/17.4) and methanol can be produced almost exclusively in the final liquid products. The extremely high value of "Selective C-C cleavage: Selective C-O cleavage" for sample 3 (13.5 wt% Zn) clearly displays its strong catalytic ability in selective breakage of C-C bond over C-O bond in the hydrogenolysis of EG. Although the overall methanol and ethanol selectivities produced from EG hydrogenolysis are not yet sufficient to justify an immediate application without further optimization in the conditions, the enhanced ability for C-C bond cleavage over C-O cleavage of PdFe with high Fe content is clearly demonstrated.

To explore the generality of this interesting catalytic property, this novel catalyst (sample 3 (13.5 wt% Zn)) was also tested for the hydrogenolysis of 1,2-propanediol (1,2-PD) and 1,2-butanediol (1,2-BD). The results are summarized in Fig. 10. In the system of 1,2-PD, ethanol (EtOH) is the product of hydrogenolytic C-C cleavage while

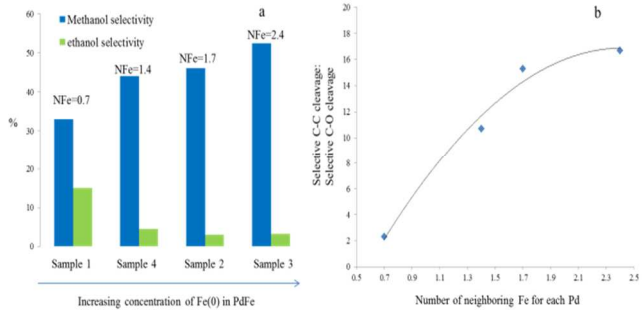

Fig. 9. a) The relationship of methanol and ethanol selectivity; b) calculated "Selective C-C cleavage: Selective C-O cleavage" value during hydrogenolysis of EG at increasing Fe content in PdFe. (NFe refers to the number of neighbour Fe around each Pd absorbing atom.)

Table 6. Catalytic performance of the supported PdFe catalysts in hydrogenolysis of ethylene glycol (EG). (0.50 g catalyst; 30 mL EG solution (5 wt%); 50 bar H_2 (r.t.); temp. = 250 °C for 24 h, the other trace products include CO, CH_4, C_2H_6, etc)

Catalyst	Conv.	Select.% CH_3OH	Select.% C_2H_5OH	Select.% CO_2	Select. cleave of C-C/C-O
Sample 1 (0.0 wt% Zn)	31.8	32.9	14.5	52.0	2.3
Sample 2 (11.8 wt% Zn)	21.0	44.7	3.0	48.3	14.9
Sample 3 (13.5 wt% Zn)	23.0	52.4	3.2	42.7	16.4
Sample 4 (20.8 wt% Zn)	18.0	44.2	4.4	47.0	10.0

("Conv." and "Select." represents "conversion", "selectivity", respectively)

1-propanol (1-PrOH) is produced by breaking C-O bond. By applying the same principle, 1-propanol is produced by the C-C bond cleavage in the hydrogenolysis of 1,2-butanediol (1,2-BD) while 1-butanol (1-BuOH) is the unique product of the C-O bond breakage. The favoured formation of terminal 1-propanol or 1-butanol over the two cases over iso-alcohols is attributed to the relative ease of –C-O hydrogenolytic cleavage at the secondary carbon than the primary carbon in the molecules presumably via carbonium ion. From the mole ratio of the products, the value of "Selective C-C cleavage: Selective C-O cleavage" can be calculated in all the systems. As shown in Table 7, the cleavage of C-C/C-O values vary from 16.4 to 3.2 and 60.3 for EG, 1,2-PD and 1,2-BD respectively. The much lower value for 1,2-PD than the other two is thought to reflect the rapid degradation of the 1,2-PD on the acidic/basic support (Zn^{2+} incorporation in support may also increase the surface properties) through the dehydration of the secondary –OH [41,42,43], which involves the formation of C=C bond with the neighbour $-CH_3$, followed by hydrogenation on metal surface to 1-propanol. The inability of C=C formation due to the absence of neighbour $–CH_3$ in EG and the steric effect of $-CH_2CH_3$ in 1,2-BD disfavours this C-O cleavage on the support and hence the high ability of the noble metal in selective C-C cleavage dominates the results. Nevertheless, these values are much larger than 1, which reveals the superior specificity of sample 3 (13.5 wt% Zn) for

selectively breaking C-C bond over C-O bond in the hydrogenolysis of 1,2 vicinal diols of this series of biomass related molecules.

Furthermore, the hydrogenolysis of glycerol over the same catalyst has also been attempted. In biodiesel synthesis, glycerol is a well-known by-product.[44] Due to its narrow range of application, glycerol is regarded as an industry waste. [45,46] Thus, the catalytic conversion of glycerol to value-added chemicals creates huge significance from both scientific and technological perspective. The catalytic result of sample 3 (13.5 wt% Zn) for glycerol hydrogenolysis is displayed in Fig. 11a. The liquid products identified are mainly composed of 1,2-PD and EtOH, accompanied by a small proportion of 1-propanol and methanol; the distribution of the liquid products is much narrower than that is catalysed by the reported[19] PdFe catalyst with a much lower Fe content (Fig. 11b). It is well accepted that glycerol can be rapidly converted into 1,2-PD through the dehydration of glycerol on a oxide support followed by a hydrogenation on metal site [41,47] (the glycerol conversion as described in Fig.11 is 100%). Further products are mainly derived from the subsequent breaking down of 1,2-PD. Taking the final selectivity of EtOH (31.5%) and 1-PrOH (6.2%) into account, the value for "Selective C-C cleavage: Selective C-O cleavage" is 7.6. This value is even higher than that (3.2) using 1,2-PD as the substrate, presumably C-C bond is readily cleaved on metal surface once 1,2-PD or derivatives are produced, with a minor effect of the dehydration of the produced diol on the support. In this case, some methanol molecules have been produced in the process of C-C cleavage. Thus, the total selectivity for small alcohol molecules, as liquid fuel products from glycerol hydrogenolysis including methanol, ethanol, is over 50% in liquid products when sample 3 (13.5 wt% Zn) is employed as the catalyst. As far as we are aware, selective catalytic hydrogenolysis of glycerol to these small alcohols as above for energy utilization has not been reported. Further extension of reaction time could further convert 1,2-PD accordingly, which then increases the selectivity of small alcohol molecules.

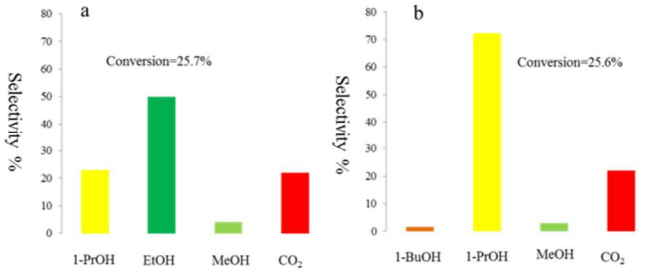

Fig. 10. Catalytic performance of sample 3 (13.5 wt% Zn) in hydrogenolysis of a) 1,2-propanediol (1,2-PD) and b) 1,2-butandiol (1,2-BD) (0.50 g catalyst; 30 mL substrate solution (5 wt%); 50 bar H_2 (r.t.); temp. = 250 °C for 24h, trace products include CO, C_2H_6, etc.).

Table 7. The calculated ratio of "Selective C-C cleavage: Selective C-O cleavage" for sample 3 (13.5 wt% Zn) in the hydrogenolysis of a series of diols.

Substrate	EG	1,2-PD	1,2-BD
Select. cleave of C-C/C-O	16.4	3.2	60.3

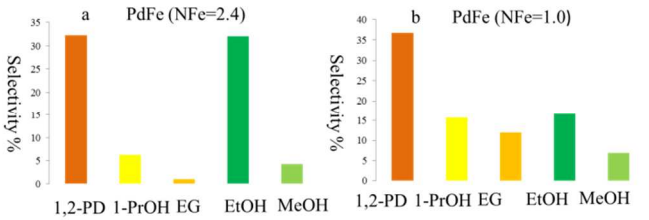

Fig. 11. Catalytic performance of a) sample 3 (13.5 wt% Zn) and b) the reported PdFe catalyst in ref. 19 in hydrogenolysis of glycerol with 100% conversion. (0.50 g catalyst; 30 mL glycerol solution (1 wt%); 50 bar H_2 (r.t.); 160 mL autoclave with stirring; temp. = 250 °C for 120 h, trace products include CO, C_2H_6, etc.)

With the combined results of characterization and catalysis, it is demonstrated that the catalytic ability of PdFe in selective C-C bond cleavage over C-O bond of vicinal diol units in the hydrogenolysis of biomass derived molecules is enhanced with a progressive increase in Fe(0) content of the bimetallic nanoparticles, which is due to the modification effect of Fe atom on the electronic structure of Pd (as shown in Fig. 7b, both the d-band filling and d-band center position shift to a lower value with increasing Fe(0) content). It is envisaged that the 1,2-diol molecule is adsorbed on the surface of PdFe bimetallic nanoparticles through the interaction of its -C-O- moiety group with the d-band of the noble metal (Scheme 2). The electron back donation from the d band of Pd to the π^* anti-bonding orbital of -C-O- will be greatly diminished with the progressive decrease in electron filling of PdFe d-band at increasing Fe substitution (Fig. 7b), which renders the hydrogenolytic C-O cleavage more sluggish. Meanwhile, the decrease in d-band filling would strengthen the electronic σ donation from the substrate to the metal, which not only enhances the Pd-C bond, but also weakens the -C-C- bond. Additionally, the PdFe with lower d-band center position at higher substitution of Fe (Fig. 7b) matches better with the weakly σ^* anti-bonding orbital of the -C-O- moiety group (as shown in scheme 2); this also promotes the σ donation from the substrate to noble metal and contributes to breaking the C-C bond. Thus, the catalytic specificity in selective C-C cleavage over C-O cleavage is gradually enhanced with the increasing content of Fe in the PdFe bimetallic nanoparticles owing to the progressive downshift in both d-band filling and d-band center position of PdFe.

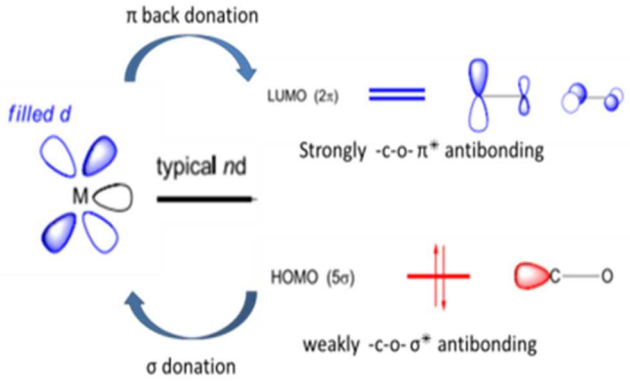

Scheme 2. Proposed interactions of Pd and -C-O- moiety group of biomass molecule.

Conclusion

Supported PdFe bimetallic nanoparticle of controllable composition can be prepared through the simple precipitation and reduction of PdO/Fe_2O_3 with the incorporation of Zn(II). The surface of the small bimetallic nanoparticles provides the active sites for the hydrogenolysis of biomass derived molecules. With increasing Fe content by tailoring the Zn(II) concentration, both the positions of d-band filling and d-band center of PdFe decrease, which strengthen the σ donation from the biomass substrate to Pd and simultaneously weaken the C-C bond. As a result, an increasing specificity for breaking C-C bond over C-O bond in diol adsorption can be achieved and this provides an exciting mean to break down biomass

compounds to small alcohol molecules with a narrow products distribution. It is also shown for the first time that this novel PdFe nanoparticle is tunable for variable degrees of C-C and C-O cleavage of a series of vicinal 1,2 diols and glycerol, which is dependent on the Fe content. This may provide a new synthesis capability for the production of small alcohols as fuel molecules from selective hydrogenolytic fragmentation of large biomass molecules.

Acknowledgements

The acknowledgements come at the end of an article after the conclusions and before the notes and references.

Notes and references

[a] Department of Chemistry, University of Oxford, Oxford, OX1 3QR, UK; E-mail: edman.tsang@chem.ox.ac.uk;

1. Y. Yu, X. Lou, and H. Wu, *Energy & Fuels,* 2008, **22,** 46–60.
2. International Energy Agency (IEA). *World Energy Outlook* 2006.
3. D. E. Bloom, *Science,* 2011, **333,** 562-569.
4. R. D. Cortright, et al. *Nature,* 2002, **418,** 964-967.
5. G. A. Olah, *Angew. Chem. Int. Ed.* 2005, **44,** 2636-2639.
6. J. Tollefson, *Nature,* 2011, **473,** 134-134.
7. G. Bolye, *Renewable Energy—Power for a Sustainable Future*, Oxford University Press: Oxford, U.K., 1996.
8. R. H. Williams, E. D Larson, R. E Katofsky, J. Chen, *Energy for Sustainable Development,* 1995, **1,** 18-34.
9. R. Hammerschlag**,** *Environ. Sci. Technol.,* 2006, ***40*****,** 1744.
10. D. Pimentel and T. W. Patzek, *Natural Resources Research,* 2005, **14,** 65-76
11. J. Zaldivar. J. Nielsen. L. Olsson, *Appl Microbiol Biotechnol* ,2001, **56,**17–34
12. R. Luque , L. Herrero-Davila, J. M. Campelo, J. H. Clark, J. M. Hidalgo, D. Luna, J. M. Marinasa and A. A. Romero, *Energy Environ. Sci.* 2008, **1,** 542 – 564.
13. M. G. Musolino, L. A. Scarpino, F. Mauriello, and R. Pietropaolo, *ChemSusChem* 2011, **4,** 1143 – 1150
14. A. V. Bridgwater, J. M. Double, *Fuel*, 1991, **70**, 1209-1224.
15. C. N. Hamelinck, A. P. C. Faaij, *J. Power Sources*, 2002, **111**, 1-22.
16. T. Chmielniak, M. Sciazko, *Appl. Energy,* 2003, **74**, 393-403.
17. E. L. Kunkes, D. A. Simonetti, R. M. West, J. C. Serrano-Ruiz, C. A. Gärtner, J. A. Dumesic, *Science,* 2008, **322**, 417-421
18. G. W. Huber, R. D. Cortright, J. A. Dumesic, *Angew. Chem. Int. Ed.* 2004, **43,** 1549-1551.
19. C. Wu, K. M. K. Yu, F. Liao, N. Young, P. Nellist, A. Dent, A. Kroner, S. C. E. Tsang, *Nature Comm.* DOI: 10.1038/ ncomms2053(2012)
20. C. Wu, J. Qu, J. Elliott, K. M. K. Yu and S. C. E. Tsang. *Phys. Chem. Chem. Phys.,* 2013, **15,** 9043-9050.
21. G. Kresse, J. Hafner, *Phys. Rev. B.* 1993, **47,** 558-561.
22. G. Kresse, J. Hafner, *Phys. Rev. B.* 1994, **49,** 14251-14269.
23. G. Kresse, J. Furthmiiller, *Comput. Mat. Sci.* 1996, **6,** 15-50.
24. P. E. Blochl, *Phys. Rev. B.* 1994, **50,** 17953-17979.
25. G. Kresse, D. Joubert, *Phys. Rev. B.* 1999, **59,** 1758-1775.
26. J. P. Perdew, K. Burke, M. Ernzerhof, *Phys. Rev. Lett.* 1996,**77,** 3865-3868.
27. J. P. Perdew , K. Burke, M. Ernzerhof. *Phys. Rev. Lett.* 1997,**78,** 1396-1396.
28. M. K. Sabbe, L. Laı´n, M. Reyniers and G. B. Marin. *Phys. Chem. Chem. Phys.* 2013, **15**, 12197-12214
29. W. Zhou, X. Hu, X. Bai, S. Zhou, C. Sun, J. Yan, and P. Chen, *ACS Appl. Mater. Interfaces,* 2011, **3,** 3839–3845
30. T. Fan, D. Pan, and H. Zhang, *Ind. Eng. Chem. Res.* 2011, **50,** 9009–9018.
31. J. Leveneur, G. I. N. Waterhouse, J. Kennedy, J. B. Metson, and D. R. G. Mitchel, *J. Phys. Chem. C,* 2011, **115**, 20978-20985.
32. S. Xuan, W. K. Hsu, D. P. Randall, V. Kotzeva and G. Z. Chen, *J. Phys. Chem. C.* 2008, **112**, 18804-18809.
33. D. Predoi, V. Kuncser, G. Filoti, G. Schinteie. *J. Optoelectronics. Adv. M.,* 2003, **5,** 211 – 216.
34. Q. Han, Z. Liu, Y. Xu, Z. Chen, T. Wang, and H. Zhang, *J. Phys. Chem. C,* 2007, **111,** 5034-5038
35. J. M. Montejano-Carrizales, et al. *Nanostruct. Mater.* 1997, **8**, 269.
36. G. Agostini, R. Pellegrini, G. Leofanti, L. Bertinetti, S. Bertarione, E. Groppo, A. Zecchina, and C. Lamberti, *J. Phys. Chem. C,* 2009, **113**, 10485–10492 .
37. S. Takenaka, Y. Shigeta, E. Tanabe, and K. Otsuka, *J. Phys. Chem. B,* 2004, **108**, 7656-7664
38. X. Yu, J. Wan, Y. Shan, K. Chen and X. Han, *Chem. Mater.* 2009, **21,** 4892–4898
39. R. E. Watson, Bennett L. H., *Phys. Rev. B,* 1978, **18**, 6439-6449.
40. D.Wang, D. Montané1, E. Chornet, *Appl. Catal. A.* 1996, **143**, 245-270
41. I. Gandarias, P. L. Ariasa, J. Requiesa, M. B. Güemeza, J. L. G. Fierrob, *Appl. Catal., B.* 2010, **97**, 248–256.
42. E. S. Vasiliadou, E. Heracleous, I. A. Vasalos, A. A. Lemonidou, *Appl. Catal., B.,* 2009, **92**, 90–99.
43. Y. Kusunoki, T. Miyazawa, K. Kunimori, K. Tomishige, *Catal. Commun.,* **2005,** 6, 645–649.
44. L. H. Hoşgun, R. Gopinath , S. N. Naik and A. K. Dalai, *Ind. Eng. Chem. Res.* **2012,** 51, 3863−3869
45. Y. Zheng, X. Chen, Y. Shen, *Chem. Rev.* **2008,** 108, 5253.
46. M. Pagliaro, R. Ciriminna, H. Kimura, M. Rossi and C. D. Pina, *Angew. Chem., Int. Ed.* **2007,** 46, 4434.
47. S. Wang, K. Yin , Y. Zhang , and H. Liu, *ACS Catal.* **2013,** 3, 2112−2121